We are IntechOpen, the world's leading publisher of Open Access books Built by scientists, for scientists

4,800
Open access books available

122,000
International authors and editors

135M
Downloads

Our authors are among the

154
Countries delivered to

TOP 1%
most cited scientists

12.2%
Contributors from top 500 universities

WEB OF SCIENCE™

Selection of our books indexed in the Book Citation Index in Web of Science™ Core Collection (BKCI)

Interested in publishing with us?
Contact book.department@intechopen.com

Numbers displayed above are based on latest data collected.
For more information visit www.intechopen.com

14

Fabrication of Planar Integrated Optic Devices by Laser Patterning

P.V.S. Marques[2,3], D. Alexandre[1,3], A. Ghasemphour[4], P. Moreira[3] and A.M.P. Leite[2]
[1]*Escola de Ciências e Tecnologia da Universidade de Trás-os-Montes e Alto Douro*
[2]*Physics and Astronomy Department, Faculty of Sciences, University of Porto*
[3]*INESC Porto, Optoelectronics and Electronic Systems Unit*
[4]*Tennessee State University*
[1,2,3]*Portugal*
[4]*USA*

1. Introduction

In recent years, there has been an intensive search of cost efficient techniques applied to integrated optic device fabrication. One approach with recognized potential is based on laser patterning upon photosensitive materials, which permits the fabrication of devices using a large material diversity and has a fast production cycle. This technique avoids the recourse to expensive and time consuming dry-etching processes, therefore reducing the cost and the processing time.
The device patterning can be achieved through large area exposure using amplitude masks or by laser direct writing with a focused laser beam. The work described here is focused on the production of devices by selective polymerization of photosensitive materials like hybrid sol-gel. In this chapter, the laser direct writing machine developed is described in detail; fabrication of lithographic masks in photosensitive photomask blanks, as well as direct-writing in hybrid sol-gel materials is also demonstrated. The fast prototyping of functional integrated optic devices that can be used as sensors, wavelength division multiplexing phased array devices and beam combiners for astronomical interferometry is demonstrated.

2. Laser direct writing

The fabrication of integrated optics (Hunsperger, 2009) follows a procedure that employs either the modification of the refractive index of materials or the deposition of layers of different materials. The objective is to create channels with a refractive index higher than that of the volume surrounding it, therefore light can be guided through a process of total internal refraction in close similarity to what happens in the case of optical fibres (Arnold, 1976).
Tridimensional definition usually requires some sort of photolithographic steps followed by a dry-etching step, making it a very time consuming and expensive process. On the case of the work described here, the devices are fabricated by laser direct writing in photosensitive materials (Marques et al., 2005), allowing the fabrication of intricate devices simply by

selective photopolymerization. In addition, the same laser direct writing process allows fast prototyping of photolithographic masks which can be used in a more conventional device fabrication procedure.

Basically, the manufacturing process consists in depositing[1] a thin film of a photosensitive material on a flat substrate, followed by selective photopolymerization of certain regions of the same film, which become resistant to the action of solvents. The aim is to use the laser beam to selectively polymerize certain regions of the film, according to the intended device pattern. This pattern appears embossed, immediately after the dissolution of the unexposed areas (which are not cured) with a suitable solvent. Therefore, the described process does not require the commonly photolithographic processes used in the manufacture of integrated devices. This method requires a laser emitting in a suitable wavelength compatible to the characteristics of the photosensitive layers. Fast prototyping can also be achieved using femtosecond pulsed lasers and non-linear multi-photon absorption.

2.1 The laser direct writing unit

The laser direct writing unit (Alexandre, 2011) is designed to work with different laser sources. A Diode Pumped Solid State Laser (DPSS) emitting at 532 nm is fitted inside the unit and is used for fast prototyping of photolithographic amplitude masks. The production of devices through photopolimerization uses an external frequency doubled argon laser emitting at 244 nm.

The laser direct writing unit has six main blocks: the optical sources, the writing beam conditioning system (acusto-optic modulator and spatial filtering), the writing head (writing lens plus writing power monitoring and control), autofocus and viewing system, sample translation stages and computer control with in-house developed software. The schematic of the laser direct writing unit is shown in Fig. 1.

The first order of the diffracted beam generated in the acusto-optic cell is aligned with the machine optical axis and is used for writing, allowing full on/off control. The control of the acoustic wave amplitude on the cell also allows dynamic control of the writing power by using a feedback control system. The optical system was designed so it could be easily converted to use one of the two available wavelengths. The quality of the beam is improved by a spatial filter (pin-hole between two plano-convex lens), at a cost of some writing power loss. The laser beam focusing objective was mounted in a vertical precision stage. Its movement is controlled by the autofocus control system or indirectly by the designed computer software.

To carry out the production of high resolution/quality devices it is necessary to ensure the uniformity and the stability of the writing beam. This implies that, in addition to the alignment, it is necessary to ensure that the writing power remains constant especially if there are power fluctuations from the laser source or mechanical drifts. A usual solution is based on a feedback circuit that can be implemented in analogical/digital form. After spatial filtering the laser beam is divided by a beam splitter, 10% to the photodetector D1, used for power monitoring and control, while the remaining power is directed to the writing lens. The autofocus system uses the writing beam reflection at the substrate. The writing beam entering the microscope objective is collimated and, if the sample is at the focal distance, the reflected beam will be also collimated. In this situation, the power received at D2 is a

[1] Deposition can be achieved by spin-coating, deep-coating, spray-coating, etc.

maximum (the opening A2 is placed in front of detector D2 and at the exact focal length of L2). When the sample is not positioned in the focal plane of the lens, the power in D2 decreases, meaning that the focus is either above or below the plane of the sample. To eliminate this ambiguity, a similar system composed by A'2, M4 and L'2 is also used. In this case, the distance between L'2 and A'2 is not exactly equal to the focal length of L'2. When the measured power decreases in D2, it is possible to determine the direction of the movement from the derivative of the signal obtained in D'2.

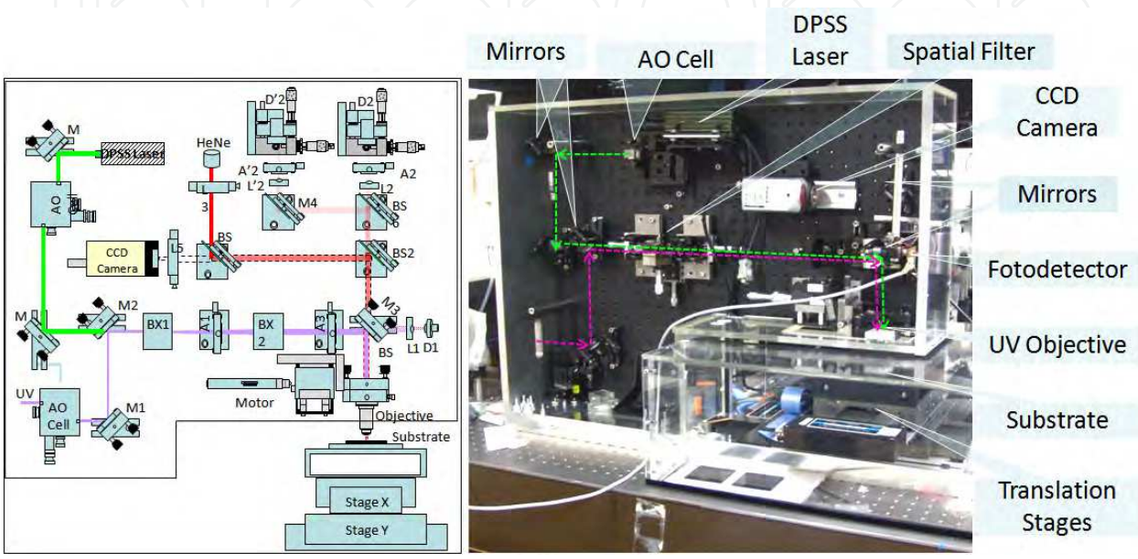

Fig. 1. In the left: laser direct writing unit schematic. In the right: the laser direct writing unit. The dashed lines indicate the optical path of each of laser beam that can be used.

The positioning of photosensitive samples is obtained through the displacement of two high resolution stages (Aerotech ABL1000), placed orthogonally, allowing separately or jointly movements in two orthogonal directions. The position is measured in absolute terms through an embedded displacement encoder, being the minimum stable displacement for both stages 25 nm (although reading resolution is 2 nm). The stages can be independently moved with speeds varying from 0 to 50000 μm/s and accelerations between 0 and 25000 μm/s^2. The minimum vertical displacement of the focusing lens positioning is 0.14 μm. The average time delay between the stop order reaching the stages and the laser beam cutting order is less than 0.1 ms, which at a speed of 2000 μm/s can induce errors up to 0.2 μm. The minimum focal diameters for the two lenses used are about 2.8 μm and 1.3 μm, respectively, to the 10 mm and 5 mm focal length lenses.

In the case of photolithographic masks writing, it is possible to watch the patterns appearing in real time since transmission is different in the exposed/unexposed areas. Monitoring is performed using back illumination with a white light source and the image obtained in the CCD camera.

To control the entire system it was necessary to build dedicated software. Fig. 2 shows the appearance of the developed application, which displays a 1x4 power splitter device to be created by laser writing. The program is able to control, separately or together, all the direct writing unit systems, manage system errors and read/interpret/execute device patterning instructions.

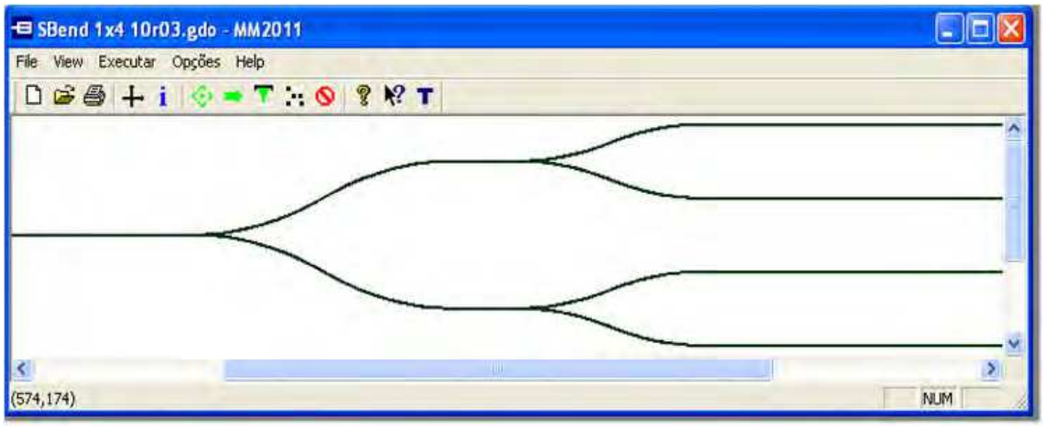

Fig. 2. Interface of the designed software. In the draw area, a 1×4 power splitter is shown.

Despite all the programmed functions it is also necessary to use external software for device design and simulation; a commercial program based on the Beam Propagation Method (Siegman, 1986) was used. After the simulation, it is necessary to convert the file describing the device design to a format that the direct writing unit software can interpret correctly. The design is exported in a bidimensional CAD file. Usually, the exported files contain only the contour information of the planned device, being necessary to use a program that interprets this information and perform the filling of the pattern as necessary, using a tool similar to the laser beam spot that will be subsequently used. It is also convenient to know the laser spot size, so that the contour is carried out within the limits of design, and also to decide the distance between centres of the parallel fill lines. The overlap factor between consecutive lines can be varied for increased uniformity. After this process, the resulting file is converted to Gerber format (Barco Gerber Systems Corporation, 1998; DiBartolomeo, 1991) which can be interpreted by the developed application. The machine control software uses the Gerber file to write the patterns on the photosensitive substrate.

3. Fabrication of photolithographic masks by laser direct writing

The photolithographic masks are produced from photomask blanks plates (Canyon Materials), which are glass plates covered by a surface layer with a high number of colour centres. A focussed laser beam can erase these colour centres due to a localized heating effect, instantaneously changing the exposed area to a transparent state. The spot size recorded in the plates is smaller than the laser spot due to a nonlinear sensitivity effect.
The first part of the direct writing process is the calibration of the energy dose required to achieve the desired patterns at the desired resolution. The energy dose (D=Energy/Area) can be controlled according to the used energy in a determined area which can be redefined in terms of the incidence power, the waveguide cross section (s) and the movement velocity (v):

$$D = P/_{s.v} \tag{1}$$

Fig. 3 shows calibrations results performed for laser direct writing on photoblank masks. In a) some transparency already exists while in c) the use of excess energy dose leads to a damaged film and a decrease of transparency.

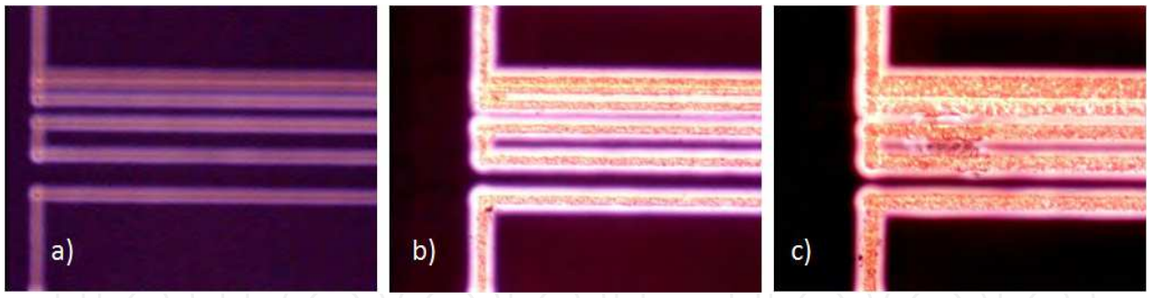

Fig. 3. Effect of writing power variation: a) 10 mW, b) 13 mW and c) 15 mW at a writing velocity of 500 μm/s.

Fig. 4 a) shows the line width achieved in a single pass when the scan velocity is 200 μm/s and the writing power is 1.7 mW.
To test the best filling conditions, squares were written using different distances between adjacent scans and/or different scan velocities. Fig. 4 b1)-b4) show the results obtained when the distances between adjacent scans range from 0.2 μm to 2.7 μm. Fig. 4 c) represents a set of straight waveguides with widths ranging from 2 μm to 10 μm, in steps of 1 μm (the distance between adjacent scan lines was 0.2 μm).

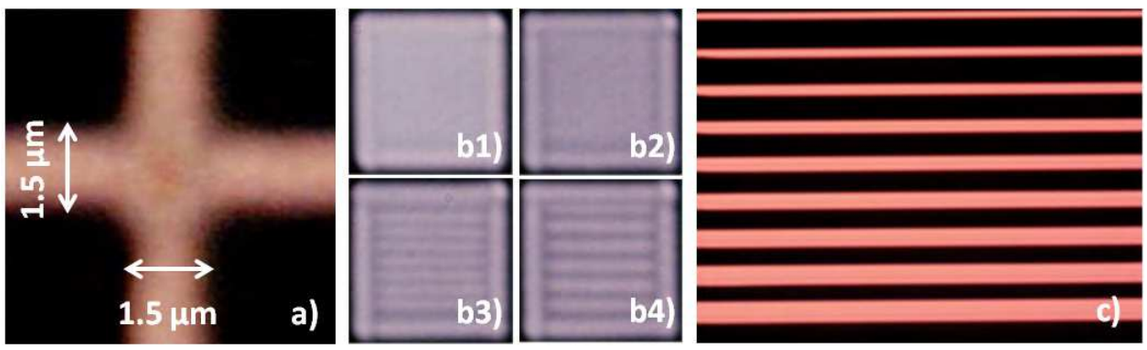

Fig. 4. Straight waveguides with widths ranging from 2.0 to 10.0 μm in 1.0 μm steps. The distance between adjacent scans was 0.2 μm in each case, the scanning velocity was 200 μm/s and the writing power was 1.7 mW.

An important aspect is the relationship that should exist between the writing speed and acceleration/deceleration, while starting/stopping the stages. The time periods in which speed is not constant depend mainly on the difference between initial and final velocities and the value of acceleration. When the stages are not properly tuned, it is usual to observe an overshoot effect (Fig. 5), because the stages have nonzero velocity as they cross the destination position. This effect can be carefully compensated through parameters calibration, for a given range of speeds, accelerations and load on the stages. After calibration, this effect becomes negligible compared to the usual devices dimensions. The figure also shows a wobble effect due to the fact that one of the stages is still positioning (in the direction orthogonal to the motion) while starting a new line after a sudden change on the movement direction. This causes fluctuations around the desired straight line, during the beginning of the writing. This problem is easily solved by inserting a short time delay before starting a new line (typically 1 ms).

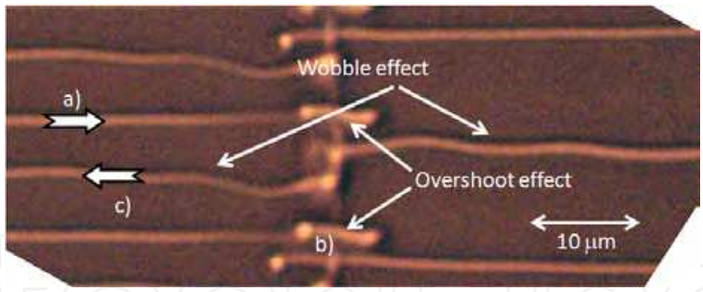

Fig. 5. a) Movement direction towards the end of a line, b) overshoot effect at the end of the line, c) movement after reversal of writing direction and lack of the stabilization period before the start of a new line. The acceleration is 5000 μm/s² and write speed is 2000 μm/s.

In some cases the photopolymerization is obtained by flood exposure by a KrF excimer laser (248 nm) through an amplitude mask. Fig. 6 shows an amplitude mask defined by laser direct writing in photomask blank. This mask was used to replicate the pattern in a NiCr metallic film deposited in a pure silica plate, through conventional photolithographic steps and NiCr wet-etching procedures. This is necessary as the photomask blanks cannot be exposed to deep UV sources, such as the KrF excimer laser, without being damaged.

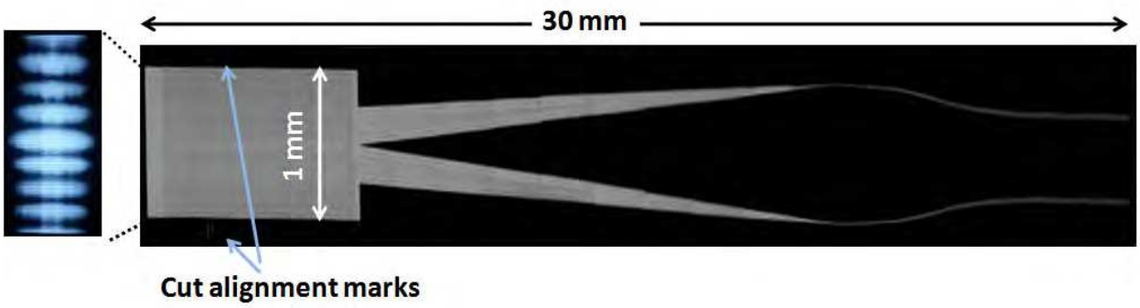

Fig. 6. Mask photograph (NiCr film on a silica substrate) replicated from a photoblank pre-mask. Outside of the free propagation zone a few marks were draw to assist in device cutting. The irregularities are due to concatenation of photographs.

3.1 Laser direct writing in hybrid sol-gel

The first step is the synthesis of the sol-gel material and the fabrication of the thin film by spinning in an appropriate substrate (usually glass or silicon). The sol-gel materials used in this work were obtained by hydrolysis and polycondensation of methacryloxypropyltrimethoxysilane (MAPTMS), to which zirconium propoxide (ZPO) mixed with methacrylic acid (MA) was added, in a suitable molar proportion, to attain the desired value of the refractive index. More details of the synthesis can be obtained in (Moreira, 2006a). The device production follows the process represented in Fig. 7.

As in the masks case, before starting the production of devices in hybrid sol-gel, it is also necessary to perform the calibration of the process, since the energy dose is a function of the incidence power and the exposure time (or movement velocity) during the writing process. The first step is the determination of the minimum amount of energy necessary to polymerize the hybrid sol-gel layer and, for that energy dose, what is the smaller feature that can be draw.

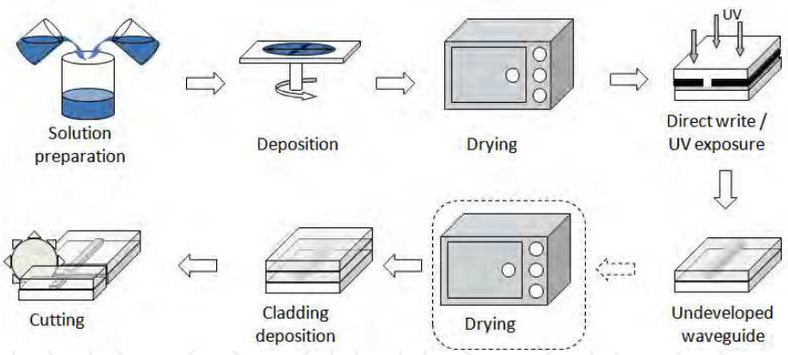

Fig. 7. Production of integrated optical devices, based on hybrid sol-gel technology, with the possibility to use (not shown) or skip the development step. The photopolymerization can be obtained by flood exposure through an amplitude mask, as represented in the figure, or by a focused laser beam (not shown).

To check the minimum line width, some lines were written while varying the writing lens position relatively to the substrate. This is conducted in an extension that ensures that at some position the beam is perfectly focused on the film. Under these conditions there is significant variation of the energy dose, which means that in positions farther from the correct focus position (above and below the optimum position), the film polymerization is not completed through the film depth, implying that it will be removed during the development step, Fig. 8. In the test performed, lines with width below 2 μm were observed.

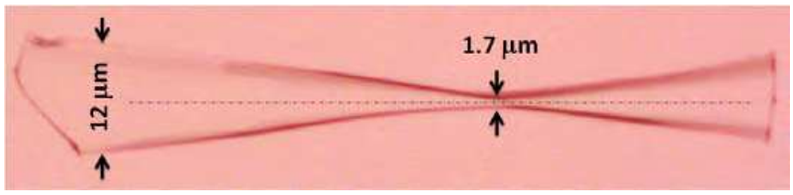

Fig. 8. Effect of the movement of the focus objective during the stages translation. The minimum width obtained for a writing power of 20 μW, a velocity of 500 μm/s and a 20× objective was 1.7 μm.

Fig. 9 shows the cross sections of the obtained structure when the focus position changes around the optimum position.

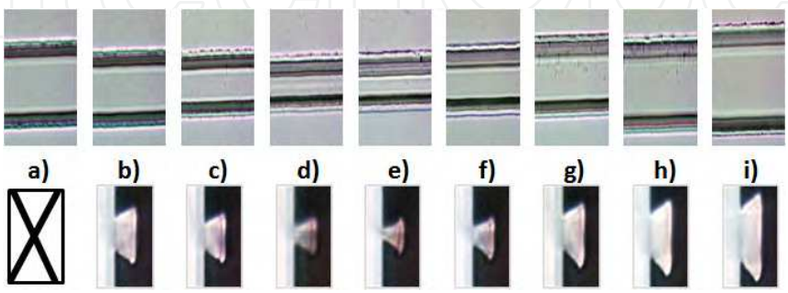

Fig. 9. Top view and cross sections of waveguides obtained by direct writing for different focus positions (20× objective used). The focus position varies approximately from -56 to +56 μm, in 14 μm intervals.

The waveguide profile is not rectangular due to the fact that energy varies across the focal cross section; the writing process is accomplished by "dragging" the laser beam on the sample. On a non-saturation regime, and assuming that the material absorption is linear, the waveguide section has about the same shape profile of the energy dose applied in the waveguide writing process (Corbett et al., 2004).
Assuming that the writing beam intensity is a Gaussian function, the energy density at any position parallel to this axis, can be obtained by integrating the distribution function for the corresponding x coordinate (assuming that the movement is in the y direction):

$$F(x) = \frac{2\int_0^{\infty} f(x,y)\partial y}{v} = \frac{\frac{\sqrt{\pi}}{\sigma\sqrt{2}} A e^{-\frac{x^2}{2\sigma^2}}}{v} \quad (2)$$

where A is the laser beam intensity. It was assumed for simplicity $(x_0, y_0) = (0, 0)$, and $\sigma_x = \sigma_y = \sigma$, which is the case of a beam with radial symmetry (valid for a properly aligned laser beam).
Fig. 10 a) shows a simulation of the profile variation for different writing powers.

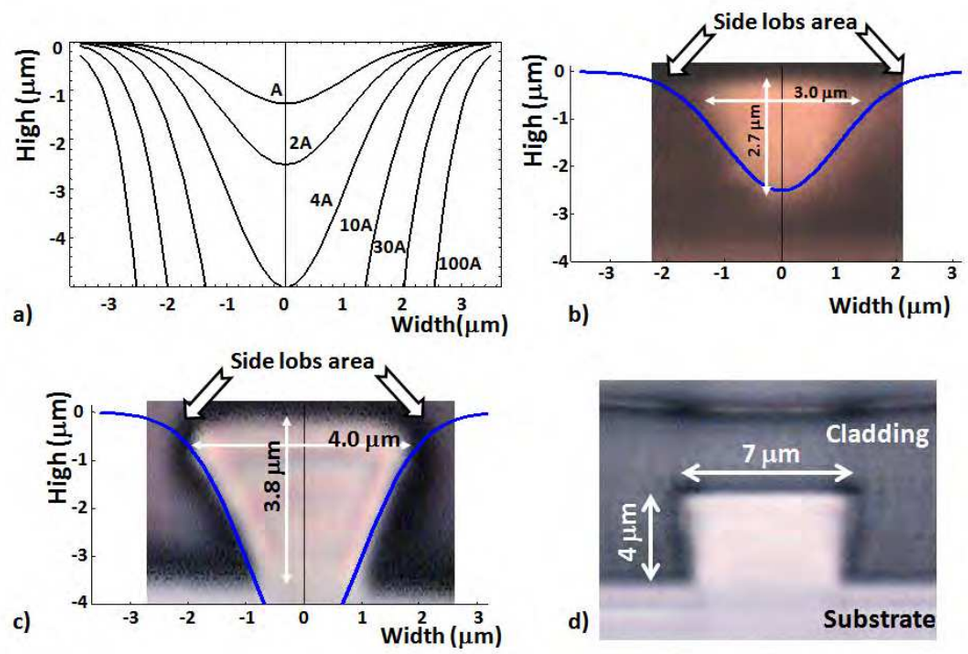

Fig. 10. a) Simulated profile of the provided energy dose as a function of the beam maximum intensity. b) and c) Waveguides written with the same power (25 μW) but with different velocities, v = 350 μm/s and v = 50 μm/s, respectively. The blue line is the energy dose profile used in the writing process. d) Section of a waveguide after the development process and the deposition of a cladding layer. The writing power was 100 μW and the velocity 50 μm/s.

Fig. 10 b) and c) shows the profile of two waveguides written at different velocities using the same writing power. It appears that the waveguide profile follows the energy dose profile

used in the waveguides polymerization. In b), the polymerization was not enough to "connect" the waveguide to the substrate at the bottom of the picture. This waveguide was not developed showing a smooth refractive index gradient from the waveguide core to its surroundings. In the case of figure c) the waveguide is developed, making it easier to determine its dimensions as the surrounding environment is air. As illustrated in Fig. 10 d), setting the writing velocity value, the power can be increased to obtain almost rectangular profile waveguides.

After the analysis on the waveguide dimensions and profile, it is also necessary to perform a calibration involving the following quantities:

- stages velocity;
- laser beam power and beam focus position relative to the sample;
- photosensitive film composition;
- overlapping between adjacent lines.

As already mentioned, there is the possibility that the photosensitive film polymerization is only superficial. When this happens, and despite the waveguides formation, during the development process these waveguides are removed, since the physical connection to the substrate is removed by dissolution. Fig. 11 shows a set of waveguides photographs where the stages velocity, the laser beam power and the writing beam focus position were varied.

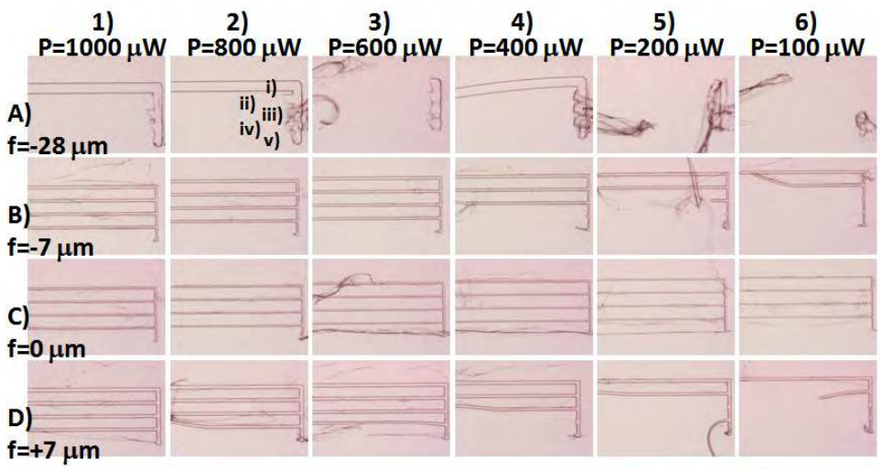

Fig. 11. Calibration of the waveguides writing process. In the rows the focus position was kept constant while in columns is the writing power that remains constant. Within each image there are (at most) 5 rows where the velocity is varied: i) 50 μm/s, ii) 100 μm/s, iii) 250 μm/s, iv) 500 μm/s and v) 1000 μm/s.

Fig. 11 shows that many of the written lines have not been sufficiently polymerized to ensure fixation to the substrate. Sometimes during the development step, these lines are shifted from their original positions, being randomly deposited in other areas of the substrate, (B5, C3, D2). At the extremes, during acceleration or braking phases, the writing velocity is lower favouring the polymerization process, i.e. the end of the waveguide remains fixed while the rest of the waveguide is moved away (4A, 6B, C3, D5). Line A in Fig. 11 shows that it is possible to write larger lines with widths above 40 μm, as shown in 1A and 2A.

The graphs in Fig. 12 were elaborated from the table of Fig. 11, allowing the evaluation of the system behaviour for the different parameters.

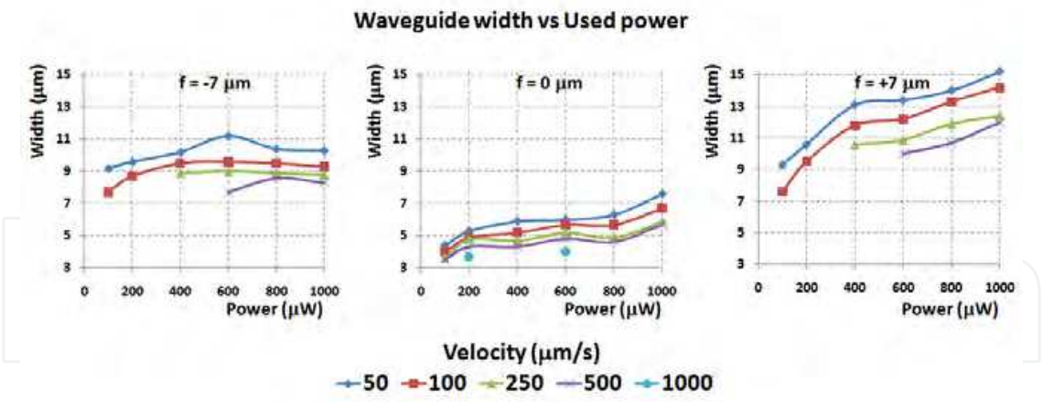

Fig. 12. Width of the waveguides made by laser direct writing as a function of the writing beam power for different focusing offsets and for different stages velocities.

Another factor that influences the quality of the fabricated devices is the structures homogeneity in terms of morphology and refractive index when these are composed of elements whose width is greater than the writing laser beam width, like found in the multimodal (MMI) device (M. Bachmann, 1994). In these cases it is necessary to perform the filling of some areas by writing successive parallel lines, overlapping the adjacent lines, while adjusting the overlap degree. Fig. 13 shows the test results performed on hybrid sol-gel by writing several parallel lines, successively closer to each other. The spacing between adjacent rows was varied between 3 µm and 10 µm, centre-to-centre, with a writing beam of about 5 µm diameter. When the spacing between the lines is less than 5 µm, the variation of the surface height is less than 0.3 µm.

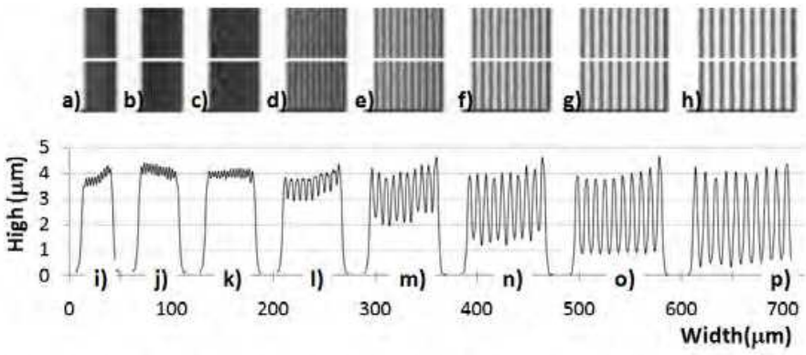

Fig. 13. Effect of separation increase between the consecutive writing lines (hybrid sol-gel). The separations used ranged from 3.0 µm to 10.0 µm with increments of 1.0 µm for figures a) through h), respectively. Figures i) to p) represents the variation of height along the indicated cuts on the white line marked in the photographs from a) to h). The writing power was 200 µW and writing velocity 50 µm/s.

The increase in the total number of writing lines has the disadvantage of increasing the device manufacturing time. However, the edges of objects tend to be more perfect, and the final dimensions more accurate.
As mentioned, the linewidth decreases with increasing velocity, which can lead to surface non-homogeneities, as illustrated in Fig. 14. A better homogeneity is obtained for lower

velocities, although it is accompanied by a slight increase in the device width, since the contour is also accomplished with a broader line. In this case, the spacing between adjacent writing lines was held constant (4.0 μm, centre-to-centre). When the writing velocity was diminished there was an increase of the applied energy dose, which implied an increase of the refractive index (polymerized areas) and hence an increase in the refractive index contrast, Fig. 14 b).

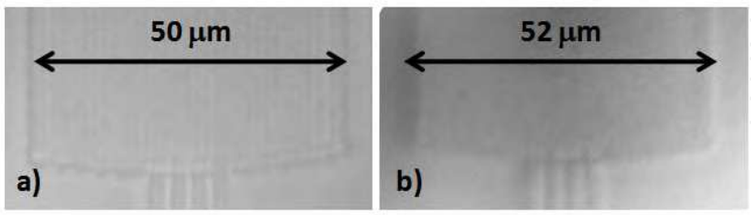

Fig. 14. Input section of two devices written using different velocities. The velocities used in a) and b) were 250 μm/s and 100 μm/s, respectively, for a 4.0 μm spacing between adjacent lines. The writing power was 100 μW.

Although it was not deeply studied, it is obvious that the filling strategy influences the performance of the device. Fig. 15 shows a device written by scanning successive lines that follow the contour of the area to fill, starting from the outside, filling in every turn the next perimeter immediately next the chosen spacing. As the direction changes, a braking/acceleration is required in these areas, leading to non-uniform areas where a higher energy dose was applied.

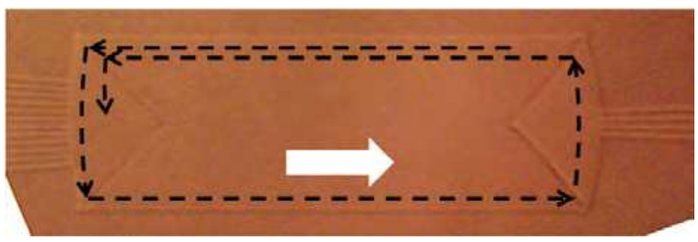

Fig. 15. Aspect of a complete symmetric, although not fully written in the propagation direction (indicated by the white arrow). The dashed lines indicate the direction and the shape of filling. The lines on the left and right are written using arc segments.

Many of the patterns used in integrated optics are curvilinear, which can be set using small line segments, but it was found that this process lead to inhomogeneities because of the pauses in the transitions between lines that define the curves. Therefore, modifications were introduced in the control program implementing the Gerber instructions that allow arcs to be drawn in one movement, instead of be accomplished by a set of linear segments. The problems that arise due to the acceleration/direction change periods are also observed at the intersection of two concatenating line segments, Fig. 16.

Another important case is the one in which the developing step is skip and the sample is thermally cured after UV exposure. On this situation, an observed refractive index difference between the UV exposed and non-exposed volumes still exist. The waveguides do not have a sharp contrast to the surrounding media since the non-exposed material is not removed, as usual, in the development step.

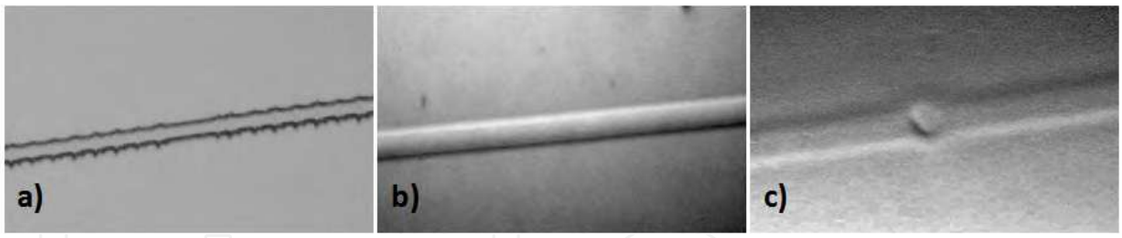

Fig. 16. Waveguides sections written in s-bend. a) Curve defined by short straight lines, b) curve defined by an arc segment, c) transition point between two adjacent line segments.

Fig. 17 shows the waveguides cross sections images written at different velocities and powers and the respective waveguides mode profile, following the manufacturing process which eliminates the development step. It appears that for lower writing powers, the drawn waveguides dimensions decrease significantly.

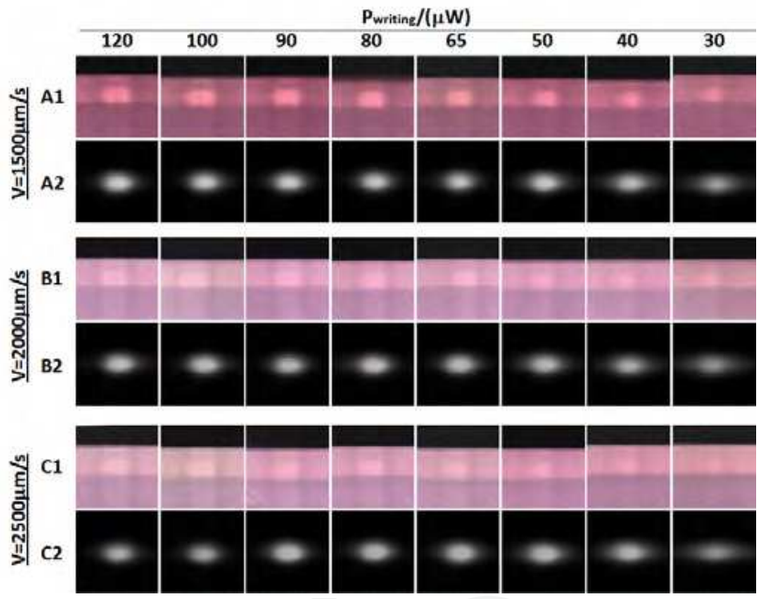

Fig. 17. Lines A1, B1 and C1: waveguides achieved by laser direct writing using the manufacturing process without development step. Lines A2, B2 and C2 are images of the waveguides modes acquired by a CCD camera (λ = 1310 nm).

Fig. 18 was obtained by processing the modal distributions included in Fig. 17, lines A2, B2 and C2. Fig. 18 a) shows the variation of normalized maximum intensity of the obtained modes for each of the produced waveguides. For the lowest writing powers, there is a decrease in the intensity representing an increase of the losses caused by an insufficient waveguide polymerization, which is more evident for waveguides written at higher velocities. Fig. 18 b) shows the variation of the propagated mode width along the horizontal direction (solid lines) and the vertical direction (dashed lines). In the horizontal direction, the mode width increases when the writing power decreases (with no noticeable dependence on the writing speed) due to a lower energy dose used in the polymerization. This produces waveguides with lower refractive index and thus with less contrast relatively to the surrounding environment, in which the mode penetrates more deeply. In the vertical

direction, the modes width is almost constant which is justified by the fact that the latter is limited mainly by the thickness of the hybrid sol-gel layers deposited.

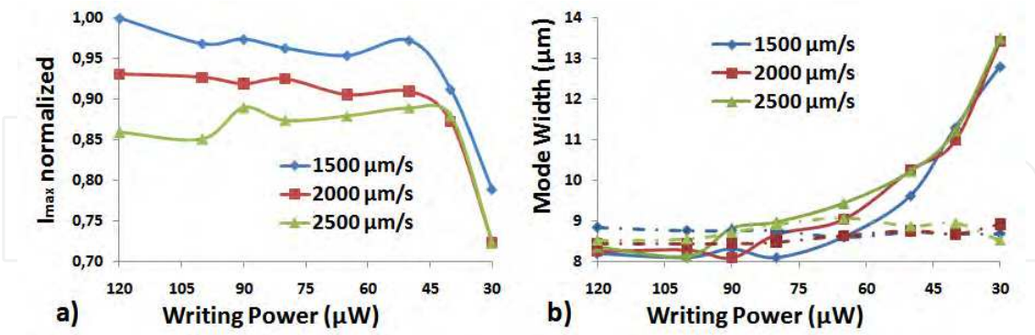

Fig. 18. a) Maximum intensity (normalized) obtained from the analysis of the images in lines A2, B2 and C2 from Fig. 17. b) Modal width (obtained at $1/e^2$ of maximum power) for the vertical direction (dashed line) and for the horizontal direction (solid line).

4. Design, fabrication and testing of functional integrated optic devices

4.1 Integrated refractive index sensor based on a Mach-Zehnder interferometer

In integrated optics there are several examples of integrated interferometers capable of measuring a wide variety of physical quantities (Alexandre et al., 2007a; Fushen et al., 1996; LukoszandStamm, 1990) and/or observe the presence of different chemical elements (Pruneri et al., 2009). The application of these devices in the biosensors field (Schmitt et al., 2007; Schwartz et al., 2006) is a rapidly developing field due to the possibility of the implementation of real time measurements without the need for more complex and indirect procedures (Marques et al., 2009).

A prototype device for refractive index measurement with high sensitivity and high dynamic range based on a Mach-Zehnder integrated interferometer was developed, Fig. 19 (Alexandre et al., 2007b).

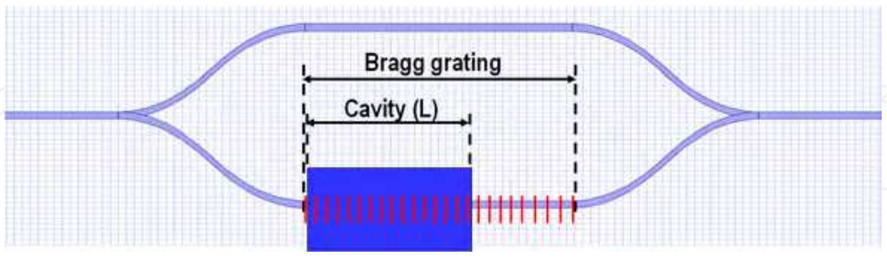

Fig. 19. Schematic of the refractive index sensor. The shaded zone represents the cavity with length L where the refractive index change will take place.

In one of the interferometer arms a Bragg grating is recorded (Kashyap, 1999; Lee, 2003) which is partially exposed through a cavity defined in the cladding of the devices. This device enables high resolution measurements from the interferometric output and high dynamic range due to the reflections of the Bragg grating inscribed in one of the Mach-Zehnder interferometer arms. Because the Bragg grating exists in two distinct sections of the device, inside and outside the cavity, the device behaves as if it has two different Bragg

gratings. This is due to the fact that, although the two sections have the same period, the effective refractive index is different in both sections. Therefore, two reflection peaks are produced at different wavelengths (with a few nanometres separation), when the waveguide is illuminated with a sufficiently broad spectrum source. Equation (2) describes the relationship between the effective refractive index of the monomode waveguide (n_{ef}), the Bragg grating period (Λ) and the Bragg wavelength (λ_B)

$$\lambda_B = 2n_{ef}\Lambda \tag{3}$$

The presence of two Bragg gratings allows exclusion of temperature effects on the device, i.e., if there is a refractive index variation in the cavity, there will be only a shift in the correspondent Bragg reflection. In the case of temperature variations, both gratings will be affected thus resolving the ambiguity, Fig. 20.

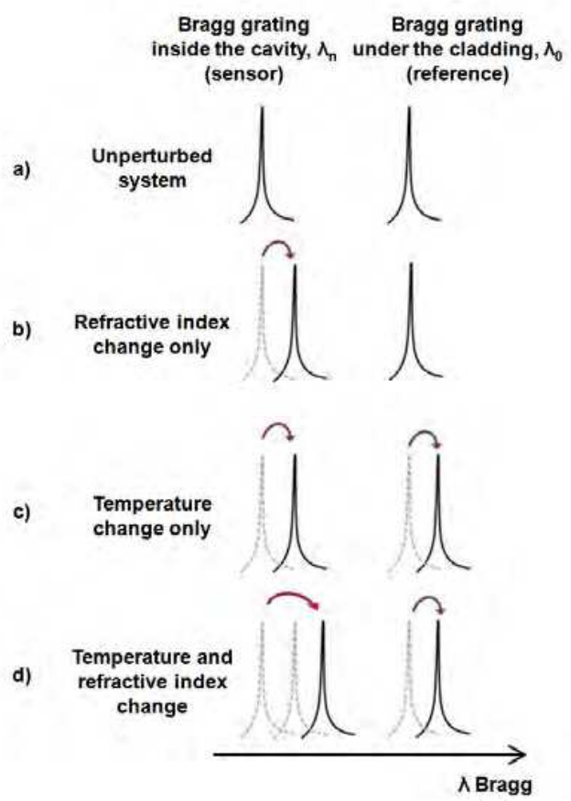

Fig. 20. Interpretation of the reflected Bragg gratings wavelengths. a) Unperturbed system; two distinct wavelengths are reflected, λ_0 and λ_n. b) There is only change in the refractive index; λ_0 remains and λ_n is changed. c) There is only change of the temperature; both λ_n and λ_0 are changed. d) There is a change in the temperature and in the refractive index; both λ_0 and λ_n are changed, as in c), and λ_n additionally suffers the alterations registered in b).

The device sensitivity depends ultimately on its physical geometry and refractive indices profile. The integrated optical devices geometry is shown in Fig. 21, where the device cross section in the cavity area is presented, with and without the device development step (before the cladding deposition and cavity definition) and outside the cavity.

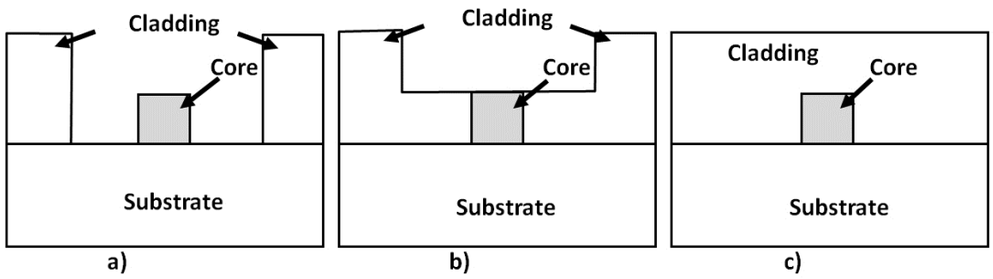

Fig. 21. Geometry of the waveguides that comprise the interferometer. a) Section of the cavity zone with the developed device. b) Waveguide inside the cavity area without development. c) Section of a waveguide in an area outside the cavities.

The separation between the two reflections, obtained from the Bragg gratings, will be proportional to the effective refractive indices difference between the cavity section and the cladding covered areas.

The device sensitivity relatively to variations in the refractive index of the material that fills the cavity is proportional to the penetration depth of the evanescent wave in the material which, in turn, depends on the refractive index contrast between the core and the surrounding material. The sensitivity also increases with refractive index contrast increase between core and substrate and with the decrease of the refractive index contrast between the core and the material filling the cavity. It should be noted that if the refractive index of the material inside the cavity is very close to the core refractive index, the guiding conditions become unfavourable, leading to higher losses and consequently to a decrease in the interferometer output visibility.

In order to maximize the interferometer output visibility, it must still be ensured that the device operates in single mode regime. It should be taken into account that the visibility will be degraded due to a power unbalance between the two interferometer arms. Additionally, in the cavity's arm, there are additional scattering losses, since the waveguide has no cladding, together with extra coupling losses at the cavity edges.

For an integrated interferometer as shown in Fig. 19, the phase difference (Δφ) between the two arms of the device for a given wavelength (λ) is given by:

$$\Delta\varphi = \varphi_{n_{ef}} - \varphi_{n_{ef'}} = \frac{2\pi L}{\lambda}\left(n_{ef} - n_{ef'}\right) \tag{4}$$

where L is the cavity length, n_{ef} is the effective refractive index of the waveguide outside the cavity and $n_{ef'}$ is the effective refractive index of the waveguide in the cavity region.

The device output power is then given by:

$$P \propto \cos^2\left(\frac{2\pi L}{\lambda}\left(n_{ef} - n_{ef'}\right)\right) \tag{5}$$

Since the parameters n_{ef} and L are fixed (determined by the device fabrication), the interferometer power output depends essentially on $n_{ef'}$.

Fig. 22 represents the variation of the effective refractive index in the cavity region, as a function of the refractive index variation of the material inserted in the cavity for the situations described in Fig. 21 a) and b).

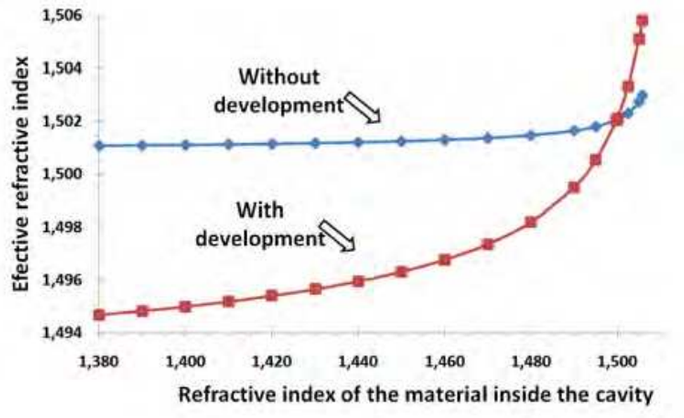

Fig. 22. Effective refractive index of the waveguide in the area of the cavity depending on the refractive index of the material (liquid) inserted into the cavity, with device development (Fig. 21 a)) and without device development (Fig. 21 b)).

Using the same parameters of Fig. 22, Fig. 23 shows, for the developed device situation, the simulation results for the normalized device power output, as a function of the refractive index of the material placed in the cavity (n_{cav}).

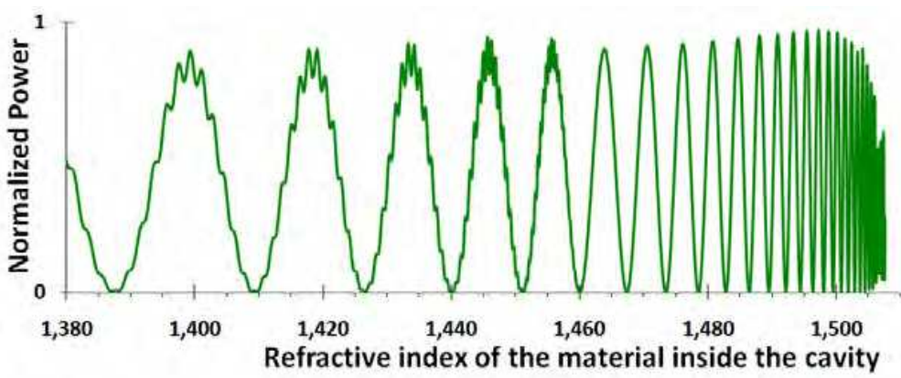

Fig. 23. Normalized interferometer output power as a function of the refractive index of the material present in the cavity.

From Fig. 22, it can be seen that as the refractive index of the material inside the cavity approaches the core material refractive index, its influence on the effective refractive index increases non-linearly (resulting that the device resolution is variable). This nonlinearity is mainly due to the fact that there is a greater penetration of the evanescent wave in the cavity material, as the refractive index difference between the core and the material inside the cavity decreases.

The devices fabricated used a development stage in which the non-exposed areas were developed away. The Bragg grating was inscribed in the waveguides using an interferometric process that employs a conventional phase mask, Fig. 24 (Kashyap, 1999).

The cladding layer was then deposited and structured to define the analysis chamber (marks were drawn in the sample to identify the limits of the Bragg grating for the subsequent alignment with the cavity). In some cases more than one cladding layer were deposited.

Fig. 25 a) shows a section of the Mach Zehnder power splitter in a device obtained by laser direct writing before the cladding deposition. Fig. 25 b) to d) contains photographs of the cavity section.

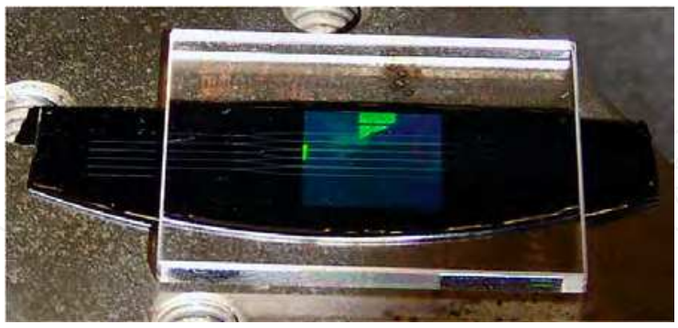

Fig. 24. Fabrication of Bragg gratings by UV exposure (KrF laser at 248 nm) through a phase mask. The major length of the diffractive area of the phase mask is 1 cm.

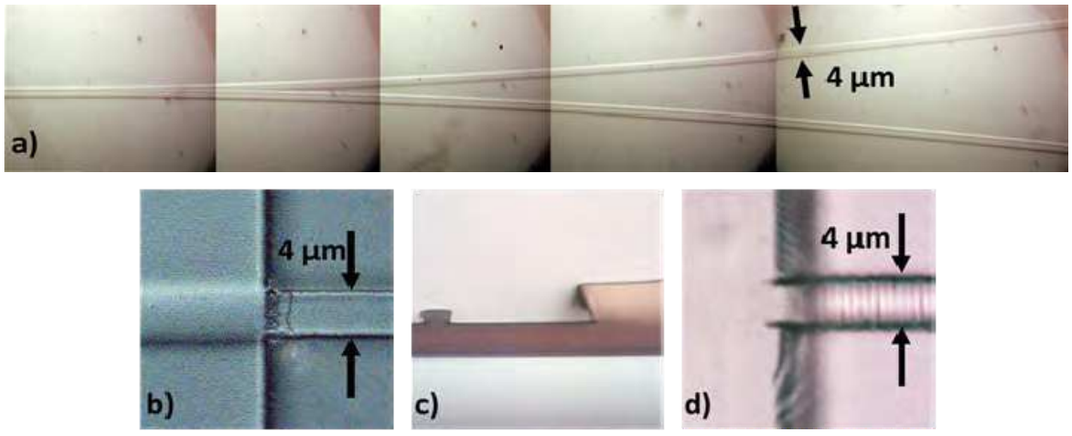

Fig. 25. a) Power splitter based on a Y junction. The width of the guides is about 4 µm. b) Waveguide interface with a thin cladding layer of ~ 7 µm. c) Cross section of a cavity containing a non-covered waveguide. d) Modulation corresponding to the Bragg grating written in the waveguide within the cavity.

The fabricated devices were tested with a tuneable laser (interferometric output) and with a broadband erbium laser source (reflection output). The reflected signal was recovered with an optical circulator placed at the input of the Mach-Zehnder interferometer.
When different fluids are introduced into the sample analysis chamber there is a clear shift in the reflected spectrum, as shown in Fig. 26 for two different liquids (after stabilization). A difference of $\Delta\lambda$ = 0.5 nm was found between the reflected central wavelengths when the cavity had only air and when the cavity was filled with an index matching oil (n = 1.380). This difference represents a change in the effective refractive index of $\Delta n \approx 5x10^{-4}$. The effective refractive index changes, observed when the index matching oil was used agree with the predicted results. However, the displacements obtained when the cavity was filled with water cannot be explained by the same equations. Also, there was an evident drift of the spectrum, taking some time to stabilize.

Fig. 27 shows the reflected central wavelength displacement as a function of time, when the cavity is filled with water. From this figure, it becomes clear that the central wavelength returns to its original value after removing the water, by an evaporation process, showing a completely reversible process.

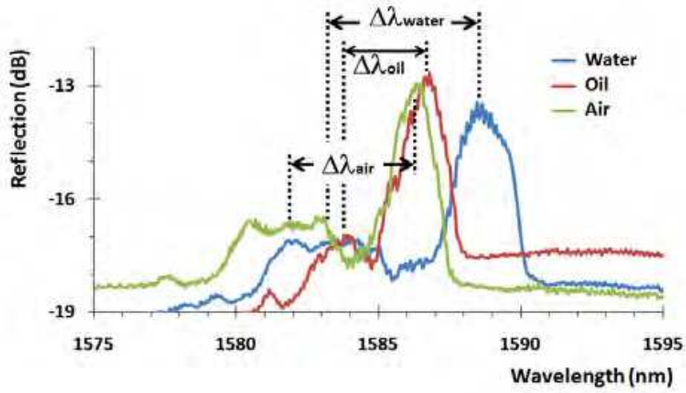

Fig. 26. Reflection of a Bragg grating with a period of 528 nm, when the cavity is filled with air (n_{ar} = 1), index matching oil (n_{oil} = 1.380) and water (n_{water} = 1.333).

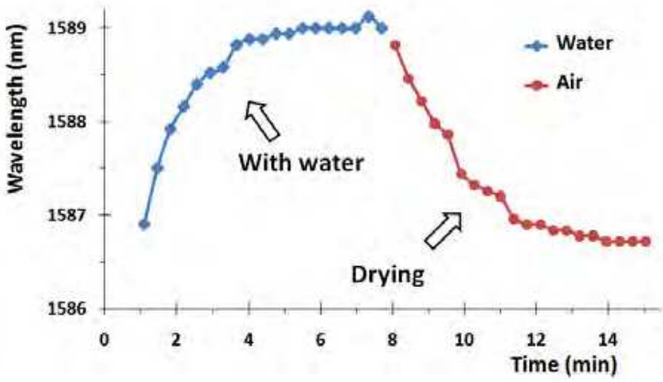

Fig. 27. Central wavelength of Bragg grating within the cavity during the stabilization period when the cavity is filled with water and then subject to a drying process.

These results indicate that there is a diffusion process to the channel waveguide, which depends on the liquid solution used, being particularly noticeable in the case of aqueous solutions. Fig. 28 shows the result obtained at the interferometric output when the cavity is filled with water. The effect of absorption and water release (through heating), had already been described (Soppera et al., 2007) in the context of the origin of propagation losses at 1.55 μm.
Fig. 29 shows the reflected wavelength variation for the Bragg grating as a function of the volumetric sugar concentration in the liquid that fill the sensor cavity.

4.2 Integrated devices for wavelength division multiplexing

The high bandwidth currently available is optical networks is partially due to the wavelength multiplexing capabilities. High density multiplexing requires complex

integrated devices that demand high quality fabrication methods as they are very sensitive to geometrical and refractive index errors. Fig. 30 shows a schematic representation of an M×N arrayed waveguide grating (AWG). The device consists of two star couplers, made by concave multimode waveguides (free propagation areas), linked by a waveguides array with equal dispersive optical length difference (ΔL) between adjacent waveguides.

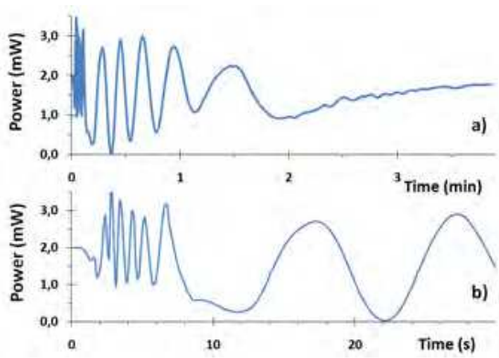

Fig. 28. a) Interferometric output measured during the insertion of a drop of water in the cavity. b) Detail of the first 30 seconds of the interferometric output presented in a).

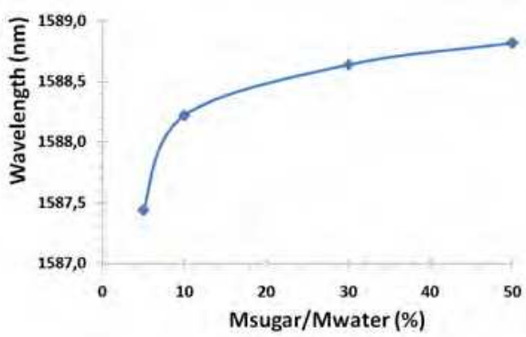

Fig. 29. Wavelength reflected by the Bragg grating when the cavity is filled with sugared water versus the mass ratio sugar/water.

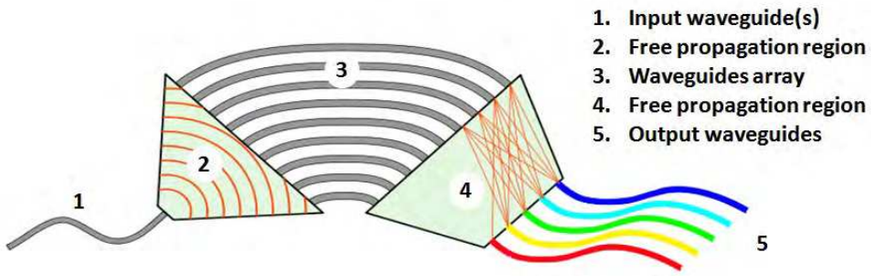

Fig. 30. Schematic representation of an M×N arrayed waveguide grating.

When the propagating beam, coming from an input waveguide, enters the free propagation region (FPR) it is no longer laterally confined. At the end of this section, the beam is coupled into the waveguides array, propagating through each of them to the second FPR. The length

of each waveguide in the array is chosen in such a way that the difference in optical path length between two adjacent waveguides equals a multiple integer (m) of the central wavelength (λ_0) of the device. For this wavelength, the fields of the various waveguides reach the output opening with the same phase (or with a difference which is a multiple integer of 2π) making the field distribution of the input opening to be reproduced in the output opening. The divergent beam into the input slot is thus transformed into a convergent beam with equal amplitude and phase distribution, and will form an image of the input field into the plane of the object in the centre of the image plane. The dispersion of the AWG is due to the linearly increasing length of the waveguides in the array, which causes the phase difference, caused by a change in wavelength in the input, to vary linearly along the output opening. As a result, the output beam is off centre and the focal point moves along the image plane as a function of wavelength. By placing receiver waveguides in suitable positions along the image plane, a spatial separation of the different wavelengths present in the radiation coupled to the device is obtained.

To demonstrate the capabilities of fast prototyping of AWG devices, some devices were simulated with a commercial program, WDM Optiwave Phasar®. The simulations were performed with the following data:

- Refractive index: Core Index of 1.511 corresponding to an effective refractive index of 1.506.
- Waveguides dimensions: 4×4 μm^2.
- Crosstalk: -20 dB.
- Central wavelength λc: 1265 nm.
- Free spectral zone: 5.2 nm.
- Channel spacing: 1.10 nm (bandwidth: 282 GHz).

Fig. 31 shows the simulated spectrum for the device under study.

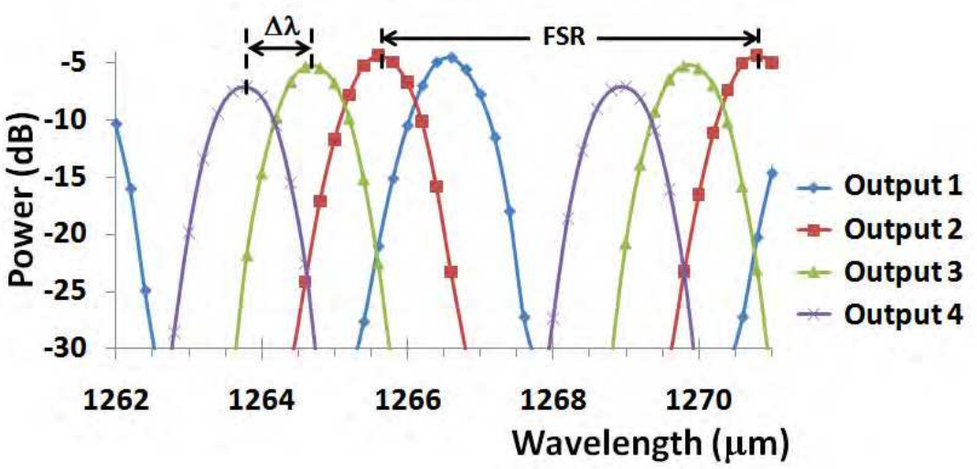

Fig. 31. Simulated spectra at the AWG device outputs when a Gaussian signal is inserted into input 1. The free spectral range (FSR) is 5.2 nm and channel spacing ($\Delta\lambda$) is 1.1 nm.

Fig. 32 shows an implemented arrayed waveguide device, where the total writing time was about 17 minutes at a velocity of 500 μm/s. As this device was fabricated without the development step, it was difficult to identify the device position after the cladding deposition. Thus, it was necessary to add some identification marks near the input and

output waveguides for easier alignment with optical fibres. Several linear waveguides were also added to evaluate the guidance conditions as well as the propagation losses.
Fig. 33 shows the free propagation zone of an AWG device implemented with four input/output channels and twelve waveguides in the array between the free propagation regions.

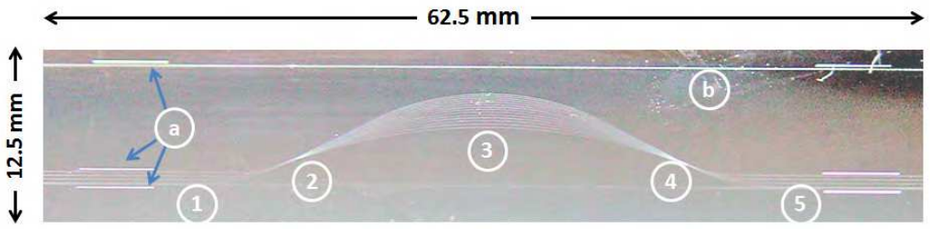

Fig. 32. Arrayed waveguide grating device before the cladding deposition (complete and at scale). a) Marks for waveguides area identification, b) linear waveguides, 1 and 5 input/output waveguides, 2 and 4 free propagating zones and 3 waveguides array.

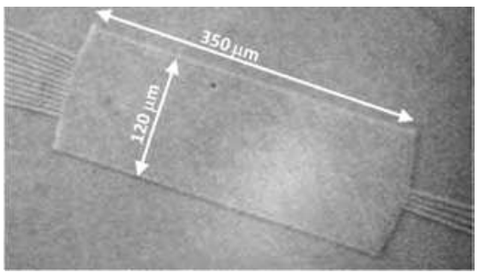

Fig. 33. Free propagation region of an AWG device. On the right are the input/output waveguides and in the left the waveguides array. The writing power was 100 µW and the writing velocity was 500 µm/s.

Fig. 34 shows the output spectrum of an AWG device when a Gaussian signal, from a SLD centred at 1265 nm, is coupled to the device with the polarization orthogonal to the device plane ($\Delta\lambda$ = 50 nm). Although the outputs are distinguishable, the crosstalk is much higher than the -20 dB expected, the best value was obtained for output channel 2 (-6.5 dB @ 1270.5 nm). The free spectral zone (FSR) is 0.4 nm larger than the expected value (5.2 nm). The results clearly demonstrate that there are phase errors but the results are promising and can be improved.

4.3 Integrated optic beam combiners for astronomical interferometry

Astronomical interferometry is an active area of research and an increasing number of new conceptual ideas and designs are being proposed to achieve optimum astronomical instruments. Long baseline astronomical interferometers allow observation with angular resolution which is one order of magnitude higher than the largest resolution available in single telescopes. In this field, integrated optics has a lot to offer in what concerns beam combination and control.
The integrated optic beam combiners can be implemented in different basic schemes (Ghasempour et al., 2008; Malbet et al., 1999). The coaxial arrangement (similar to the

Michelson interferometer configuration) can be implemented through a cascade of Y-junctions and broadband directional couplers for field separation and combination. The multiaxial combinator (Fizeau like interferometer) can be implemented by approximately collimated propagation in planar waveguides sections with the various telescopes angularly coded according to the propagation axis. Fig. 35 shows the two basic schemes of beam combiners.

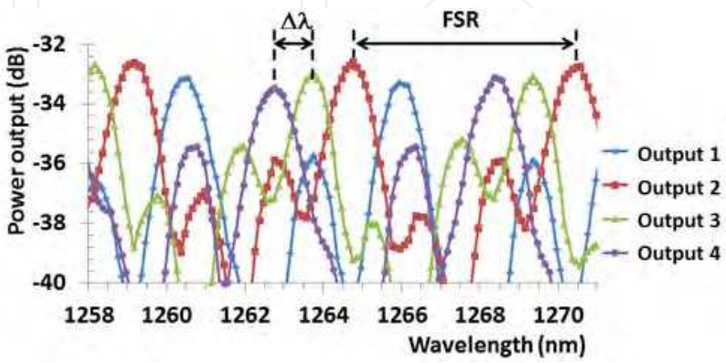

Fig. 34. Arrayed waveguide grating output spectra when an input signal (SLD with a central wavelength of 1265 nm and $\Delta\lambda$ = 50 nm) is coupled to the input. The free spectral range (FSR) is 5.6 nm and channel spacing $\Delta\lambda_{12}$, $\Delta\lambda_{23}$, $\Delta\lambda_{34}$ are 1.2 nm, 1.0 nm and 1.0 nm respectively.

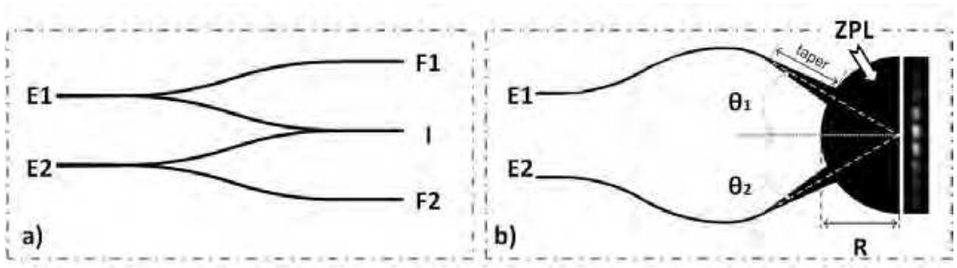

Fig. 35. Schematic drawing of a two beams combiner: a) coaxial with photometric outputs and b) multiaxial. In the case of the multiaxial beam combiner, the fringe pattern is a real example of the interference image obtained. Adapted from (Khordoni, 2010).

In both cases E1 and E2 are the inputs of the two beams to be combined. In a), both the interferometric (temporal) and the two photometric outputs are shown (the photometric outputs are used to correct the interferogram if the power collected by the several telescopes is not equal). In the multiaxial combiner, case b), the photometric outputs could also have been added. The semi-circular area with radius R corresponds to the free propagation zone (ZPL). In this region the propagation of light is confined only in the direction perpendicular to the device plane. The waveguides must end on the ZPL perimeter and are adiabatically expanded (by tapers), adapting each waveguide mode to the ZPL mode, originating an approximately collimated beam inside the interference region.

There is interest in increasing the number of combined telescopes in order to increase the interferometric systems resolution, which can be achieved through a configuration that allows more inputs combination. Fig. 36 presents as an example a three coaxial beam combiner.

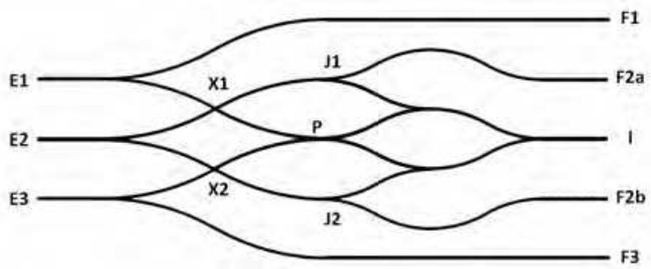

Fig. 36. Schematic of a three beams coaxial combiner with photometric outputs. X1 and X2 are crossed intersections of the waveguides. Adapted from (Khordoni, 2010).

One aspect that should be taken into consideration is the fact that it is necessary to match the different optical paths from each input to the interferometric output due to the fact that, in general, geometrically equal paths may not be optically equal. For example, the paths from E1 to I and E2 to I, although geometrically equivalent, are not optically equal as the first route passes through an extra reverse Y junction at point P, since the waveguide in this region is wider, this implies a higher optical path. To compensate for this difference the junctions J1 and J2 may be adiabatically enlarged (Moreira, 2006b).
Besides the masks production for multi-axial devices fabrication by laser direct writing, two and three coaxial beam combiners were also prepared by laser direct writing in hybrid sol-gel. Fig. 37 shows a coaxial two beam combiner where E1 and E2 are the beam combiner inputs, F1 and F2 the photometric outputs and I is the interferometric output.

Fig. 37. Coaxial two beam combiner obtained by photographs stitching.

The two devices were subsequently tested in a special characterization bench(Ghasempour et al, 2010). Fig. 38 shows the obtained interferogram for the two beam combiner, after normalization and correction using the photometry signals. Fig. 39 shows the obtained interferograms for the three-beam combiner when the inputs are combined in pairs.

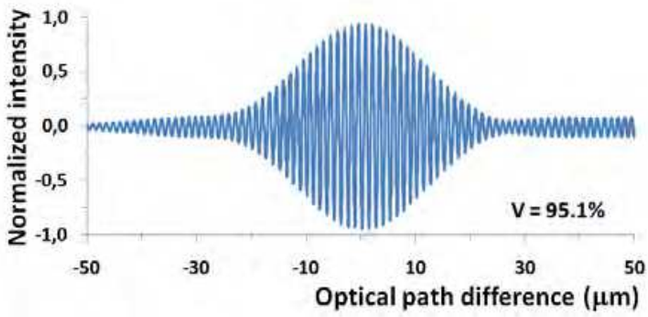

Fig. 38. Normalized and corrected interferogram obtained from the interferometric output of the two beams combiner. The obtained fringes visibility was 95.1%.

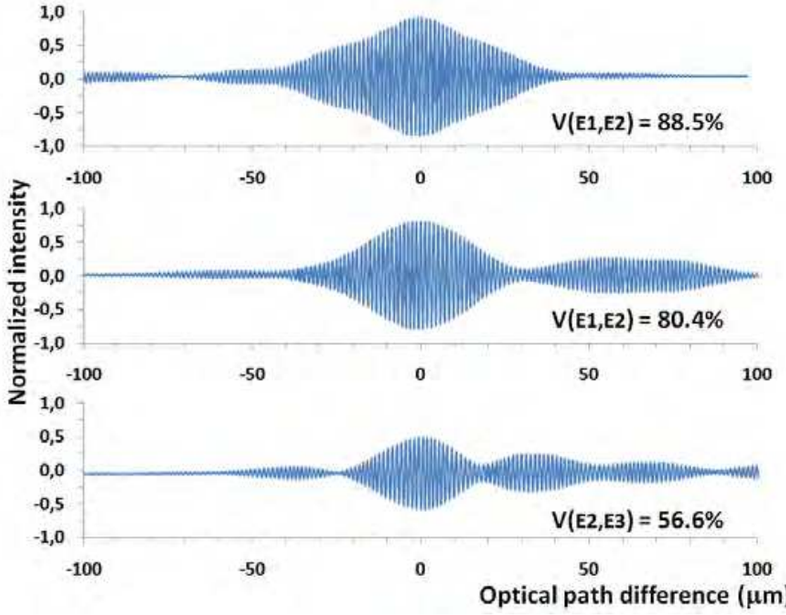

Fig. 39. Normalized and corrected interferograms obtained from the interferometric output of the three beam combiner. The obtained fringe visibility was 88.5%, 80.4% and 56.6% for the (E1, E2), (E1, E3) and (E2, E3) pairs, respectively.

Although the obtained visibilities are less than others already published (Khordoni, 2010), the obtained values, in the case of the two beam combiner, are approximately equal. In the case of the three-beam combiner, the differences are mainly due to some noticeable degradation in the tested device. Fig. 40 shows the comparison between the values for devices manufactured by standard methods involving flood exposure through amplitude masks (Ghasempour et al., 2010) and devices obtained by laser direct writing.

Combinador	Combinated pair	Visibility (masks)	Visibility (direct write)
2 beams	(E1,E2)	98.7%	95.1%
3 beams	(E1,E2)	98.1%	88.5%
3 beams	(E1,E3)	95.1%	80.4%
3 beams	(E2,E3)	95.8%	56.6%

Fig. 40. Fringes visibilities obtained for two and three beams coaxial combiners manufactured through masks replication (Khordoni, 2010) and using the laser direct writing process.

5. Conclusion

This chapter described the structure and characteristics of a laser direct writing unit that can operate at two different wavelengths, and which can be used for photolithographic masks production and direct writing on photosensitive materials. To demonstrate its capabilities three different types of integrated optic devices were produced in hybrid sol-gel for application in optical sensing, optical communications and astronomical interferometry. In some cases the

performance of these devices is slightly lower than the ones produced by conventional means but this technique is still very useful in the demonstration of practical concepts.
An interesting aspect is the possibility of device correction or addition of other elements, both in masks and in devices that are defective or incomplete; the devices can be characterized simultaneously while in a correction process. This point was not explored in this work.

6. Acknowledgments

The financial support of Fundação para a Ciência e Tecnologia (FCT) and POCI with funds from the European Union programme FEDER through projects PTDC/CTM/72093/2006, PTDC/CTM/64235/2006 and grants SFRH/BD/24493/2005, SFRH/BD/39284/2007, is gratefully acknowledged. European cost project MP0604 is also acknowledged.

7. References

Alexandre, D., Viegas, J., Fernandes, L., Moreira, P.J., Leite, A.M.P., Santos, J.L. & Marques, P.V.S. (2007a). Fabrication and Test of an Integrated Optical Sensor with High Sensitivity and High Dynamic Range Based on a Mach-Zehnder Interferometric Configuration. In: *Optical Sensing Technology and Applications*, Baldini, F., Homola, J., Lieberman, R. A. & Miler, M., pp. (U168-U179), Spie-Int Soc Optical Engineering, 0277-786X - 978-0-8194-6713-3, Bellingham

Alexandre, D., Viegas, J., Fernandes, L., Moreira, P.J., Leite, A.M.P., Santos, J.L. & Marques, P.V.S. Fabrication and Test of an Integrated Optical Sensor with High Sensitivity and High Dynamic Range Based on a Mach-Zehnder Interferometric Configuration, *Proceedings of Optical Sensing Technology and Applications*, 9780819467133, Prague, Czech Republic, April, 2007

Alexandre, D. (2011). Dispositivos Ópticos Integrados Por Escritya Directa Em Sol-Gel Híbrido, PhD Thesis, Departamento de Fisica e Astronomia da Faculdade de Ciências da Universidade do Porto

Arnold, J.A. *Beam and Fiber Optics,* Academic Press, 0120633507, New York

Corbett, S., Strole, J., Johnston, K., Swenson, E. & Weixiong, L. (2004). Laser Direct Exposure of Photodefinable Polymer Masks Using Shaped-Beam Optics. *Electronics Packaging Manufacturing, IEEE Transactions on*, Vol. 28, No. 4, pp. 312-321, 1521-334X

Barco Gerber Systems Corporation. (1998). *Gerber Rs-274x Format (User's Guide)*

Dibartolomeo, S. D-Codes, Apertures & Gerber Plot Files, Available from: http://www.artwork.com/gerber/appl2.htm

Fushen, C., Qu, L., Yunqi, L. & Yu, X. (1996). Integrated Optical Interferometer Gas Sensor. *Microwave and Optical Technology Letters*, Vol. 11, No. 4, pp. 213-215,

Ghasempour, A., Alexandre, D., Brites, C., Moreira, P.J., Reynaud, F., Marques, P.V.S., Leite, A.M.P. & Garcia, P.J.V. (2008). Rapid Prototyping of Integrated Sol-Gel Devices for Astronomical Interferometry - Art. No. 701317. In: *Optical and Infrared Interferometry*, Scholler, M., Danchi, W. C. & Delplancke, F., pp. (1317-1317), Spie-Int Soc Optical Engineering, 0277-786X - 978-0-8194-7223-6, Bellingham

Ghasempour, A., Leite, A.M.P., Alexandre, D., Reynaud, F., Marques, P.V.S., Garcia, P.J.V. & Moreira, P.J. (2010). Performance of Astronomical Beam Combiner Prototypes Fabricated by Hybrid Sol-Gel Technology. *Optics Express*, Vol. 18, No. 9, pp. 9413-9422, 1094-4087

Hunsperger, R.G. Integrated Optics: Theory and Technology, Springer, 978-0-387-89774-5

Kashyap, R. *Fiber Bragg Gratings,* Academic Press, 9780124005600, New York

Khordoni, A.G. (2010). *Guided Optics for Astronomical Interferometry*, PhD Departamento de Física e Astronomia da Faculdade de Ciências da Universidade do Porto

Lee, B. (2003). Review of the Present Status of Optical Fiber Sensors. *Optical Fiber Technology*, Vol. 9, No. 2, pp. 57-79, 1068-5200

Lukosz, W. & Stamm, C. (1990). Integrated Optical Interferometer as Relative Humidity Sensor and Differential Refractometer. *Sensors and Actuators A: Physical*, Vol. 25, No. 1-3, pp. 185-188, 0924-4247

M. Bachmann, P.A.B., H. Melchior. (1994). General Self-Imaging Properties in Nxn Multimode Interference Couplers Including Phase Relations. *Applied Optics*, Vol. 33, No. 18, pp. 3905-3911

Malbet, F., Kern, P., Schanen-Duport, I., Berger, J.P., Rousselet-Perraut, K. & Benech, P. (1999). Integrated Optics for Astronomical Interferometry I. Concept and Astronomical Applications. *Astronomy & Astrophysics Supplement Series*, Vol. 138, No. 1, pp. 135-145

Marques, P.V.S., Moreira, P.J., Alexandre, D., Melo, M., Schmidt, T.E.A., Muenzner, R., Leite, A.M.P. & Aitchison, J.S. (2005). Photosensitive Materials for Integrated Optic Applications. *Fiber and Integrated Optics*, Vol. 24, No. 3-4, pp. 10

Marques, P.V.S., Ghasempour, A., Alexandre, D., Reynaud, F., Garcia, P.J.V., Leite, A.M.P. & Ieee. (2009). Integrated Hybrid Sol-Gel Devices for Astronomical Interferometry, IEEE, 978-1-4244-4825-8

Moreira, P.J. (2006). *Integrated Optical Beam Combiners by Hybrid Sol-Gel Technology*, INESC, Technical report

Pruneri, V., Riziotis, C., Smith, P.G.R. & Vasilakos, A. (2009). *Fiber and Integrated Waveguide-Based Optical Sensors*, Retrived from http://downloads.hindawi.com/journals/js/2009/171748.pdf

Schmitt, K., Schirmer, B., Hoffmann, C., Brandenburg, A. & Meyrueis, P. (2007). Interferometric Biosensor Based on Planar Optical Waveguide Sensor Chips for Label-Free Detection of Surface Bound Bioreactions. *Biosensors and Bioelectronics*, Vol. 22, No. 11, pp. 2591-2597, 0956-5663

Schwartz, M.P., Alvarez, S.D. & Sailor, M.J. (2006). Porous SiO_2 Interferometric Biosensor for Quantitative Determination of Protein Interactions: Binding of Protein a to Immunoglobulins Derived from Different Species. *Analytical Chemistry*, Vol. 79, No. 1, pp. 327-334, 0003-2700

Siegman, A.E. *Lasers* University Science Books, 9780935702118

Soppera, O., Moreira, P.J., Marques, P.V.S. & Leite, A.P. (2007). Influence of Temperature and Environment Humidity on the Transmission Spectrum of Sol-Gel Hybrid Channel Waveguides. *Optics Communications*, Vol. 27, No. pp. 430-435

Rapid Prototyping Technology - Principles and Functional Requirements

Edited by Dr. M. Hoque

ISBN 978-953-307-970-7
Hard cover, 392 pages
Publisher InTech
Published online 26, September, 2011
Published in print edition September, 2011

Modern engineering often deals with customized design that requires easy, low-cost and rapid fabrication. Rapid prototyping (RP) is a popular technology that enables quick and easy fabrication of customized forms/objects directly from computer aided design (CAD) model. The needs for quick product development, decreased time to market, and highly customized and low quantity parts are driving the demand for RP technology. Today, RP technology also known as solid freeform fabrication (SFF) or desktop manufacturing (DM) or layer manufacturing (LM) is regarded as an efficient tool to bring the product concept into the product realization rapidly. Though all the RP technologies are additive they are still different from each other in the way of building layers and/or nature of building materials. This book delivers up-to-date information about RP technology focusing on the overview of the principles, functional requirements, design constraints etc. of specific technology.

How to reference

In order to correctly reference this scholarly work, feel free to copy and paste the following:

P.V.S. Marques, D. Alexandre, A. Ghasemphour, P. Moreira and A.M.P. Leite (2011). Fabrication of Planar Integrated Optic Devices by Laser Patterning, Rapid Prototyping Technology - Principles and Functional Requirements, Dr. M. Hoque (Ed.), ISBN: 978-953-307-970-7, InTech, Available from: http://www.intechopen.com/books/rapid-prototyping-technology-principles-and-functional-requirements/fabrication-of-planar-integrated-optic-devices-by-laser-patterning

INTECH
open science | open minds

InTech Europe
University Campus STeP Ri
Slavka Krautzeka 83/A
51000 Rijeka, Croatia
Phone: +385 (51) 770 447
Fax: +385 (51) 686 166
www.intechopen.com

InTech China
Unit 405, Office Block, Hotel Equatorial Shanghai
No.65, Yan An Road (West), Shanghai, 200040, China
中国上海市延安西路65号上海国际贵都大饭店办公楼405单元
Phone: +86-21-62489820
Fax: +86-21-62489821

IntechOpen